DOI: 10.1002/chem.200701563

# Density Functional Theory Study of *trans*-Dioxo Complexes of Iron, Ruthenium, and Osmium with Saturated Amine Ligands, *trans*-$[M(O)_2(NH_3)_2(NMeH_2)_2]^{2+}$ (M = Fe, Ru, Os), and Detection of $[Fe(qpy)(O)_2]^{n+}$ ($n$ = 1, 2) by High-Resolution ESI Mass Spectrometry[**]

**Glenna So Ming Tong, Ella Lai-Ming Wong, and Chi-Ming Che*[a]**

**Abstract:** Density functional theory (DFT) calculations on *trans*-dioxo metal complexes containing saturated amine ligands, *trans*-$[M(O)_2(NH_3)_2(NMeH_2)_2]^{2+}$ (M = Fe, Ru, Os), were performed with different types of density functionals (DFs): 1) pure generalized gradient approximations (pure GGAs): PW91, BP86, and OLYP; 2) meta-GGAs: VSXC and HCTH407; and 3) hybrid DFs: B3LYP and PBE1PBE. With pure GGAs and meta-GGAs, a singlet d$^2$ ground state for *trans*-$[Fe(O)_2(NH_3)_2(NMeH_2)_2]^{2+}$ was obtained, but a quintet ground state was predicted by the hybrid DFs B3LYP and PBE1PBE. The lowest transition energies in water were calculated to be at $\lambda \approx 509$ and 515 nm in the respective ground-state geometries from PW91 and B3LYP calculations. The nature of this transition is dependent on the DFs used: a ligand-to-metal charge-transfer (LMCT) transition with PW91, but a $\pi(Fe-O) \rightarrow \pi^*(Fe-O)$ transition with B3LYP, in which $\pi$ and $\pi^*$ are the bonding and antibonding combinations between the $d_\pi(Fe)$ and $p_\pi(O^{2-})$ orbitals. The Fe$^{VI/V}$ reduction potential of *trans*-$[Fe(O)_2(NH_3)_2(NMeH_2)_2]^{2+}$ was estimated to be +1.30 V versus NHE based on PW91 results. The $[Fe(qpy)(O)_2]^{n+}$ (qpy = 2,2′:6′,2″:6″,2‴:6‴,2⁗-quinquepyridine; $n$ = 1 and 2) ions, tentatively assigned to dioxo iron(V) and dioxo iron(VI), respectively, were detected in the gas phase by high-resolution ESI-MS spectroscopy.

**Keywords:** density functional calculations · electronic structure · high-valent compounds · iron · oxo ligands

## Introduction

High-valent iron oxo complexes are postulated to be key reactive intermediates in many biological oxidation reactions mediated by both heme and non-heme enzymes.[1–7] The electronic properties of non-heme Fe$^{IV}$=O complexes was the subject of debate, but over the past several years a number of cationic mononuclear Fe$^{IV}$=O complexes have been structurally characterized.[8–12] Recent experimental investigations and DFT calculations revealed that the reactive intermediate in the oxidation of hydrocarbons by $[Fe^{II}(TPA)]^{2+}$ (TPA = tris(2-pyridylmethyl)amine) could be Fe$^{V}$=O,[13,14] and it was noted that the reactivity of the chemically generated Fe$^{IV}$=O species was not compatible with that of iron-containing enzymes.[15] Reactive iron(v) oxo complexes with macrocyclic corrole[16] and tetraamido[17] ligands have been reported recently. However, despite these advances, no iron(VI) oxo complexes have been experimentally characterized apart from the tetrahedral $Fe^{VI}O_4^{2-}$ anion.[18–21] Theoretical calculations by Dey and Ghosh revealed that $[Fe^{VI}(O)(Cor)X]$ (Cor = corrole, X = suitable monoanionic ligand) should be experimentally detectable on the basis of the clean and significant HOMO–LUMO gaps of $[Fe^{VI}(N)(Cor)]$ and $[Fe(N)(Por)(F)]$ (Por = porphyrin) in their DFT optimized singlet states.[22]

The chemistry of the ground and excited states of both *trans*-dioxo ruthenium(VI) and *trans*-dioxo osmium(VI) complexes have been extensively studied over recent decades; the dioxo ruthenium(VI) complexes are usually reactive towards oxidation of organic compounds,[23–27] whereas the dioxo osmium(VI) complexes are strong oxidants on light irradiation.[28] One might expect that the corresponding *trans*-dioxo iron(VI) complexes, if they exist, would be more

---

[a] Dr. G. S. M. Tong, Dr. E. L.-M. Wong, Prof. Dr. C.-M. Che
Department of Chemistry and Open Laboratory of Chemical Biology
of the Institute of Molecular Technology
for Drug Discovery and Synthesis
The University of Hong Kong, Pokfulam Road (Hong Kong)
Fax: (+852) 2857-1586
E-mail: cmche@hku.hk

[**] qpy = 2,2′:6′,2″:6″,2‴:6‴,2⁗-quinquepyridine.

Supporting information for this article is available on the WWW under http://www.chemeurj.org/ or from the author.

reactive than their Ru and Os counterparts. Recently, an octahedral cationic Fe$^{VI}$≡N complex was synthesized by photochemical means and characterized by Mössbauer and X-ray absorption spectroscopies.[29] We pose the question: would a cationic *trans*-dioxo iron(VI) complex be a stable entity? As part of our efforts to study the spectroscopic and redox properties of reactive d$^2$ *trans*-dioxo metal complexes in both ground and excited states, we set out to determine their electronic structures by using DFT. In general, DFT provides excellent descriptions of the electronic structures of a variety of high-valent Fe complexes.[30–32] It has also been successfully applied to study the electronic structures of d$^2$ dioxo metal complexes of the second- and third-row transition metals, which include Mo, Tc, W, Re, Ru, and Os.[33–35] After completion of this computational work, we were able to detect the $[Fe(qpy)(O)_2]^{n+}$ ions (qpy = 2,2′:6′,2″:6″,2‴:6‴,2⁗-quinquepyridine; $n = 1$, 2) in the gas phase by high-resolution electrospray ionization mass spectrometry (ESI-MS).

## Results and Discussion

As the focus of the present work is on the electronic structure of *trans*-dioxo iron(VI) and its spectroscopic and redox properties, we performed calculations on *trans*-$[Fe(O)_2(NH_3)_2(NMeH_2)_2]^{2+}$ using several commonly used DFs and two different basis set sizes (6-31G* and 6-311+G*). The optimized structures obtained for each spin state using the same DF, but different basis set sizes are within 0.013 Å and 3° for the bond lengths and angles, respectively. Hence, herein, we present the DFT results with only the 6-31G* basis set (DF/6-31G*) (for the structures optimized with different DFs and the 6-311+G* basis set, see Table S32 in the Supporting Information).

**Relative spin-state energetics of *trans*-$[Fe(O)_2(NH_3)_2(NMeH_2)_2]^{2+}$ with different DFs**: The optimized geometries and the relative energies of *trans*-$[Fe(O)_2(NH_3)_2(NMeH_2)_2]^{2+}$ in various spin states for different DFs are presented in Table 1.

Except for the hybrid DFs B3LYP and PBE1PBE, which predicted a quintet ground state, both pure GGAs and meta-GGAs gave a singlet ground state for *trans*-$[Fe(O)_2(NH_3)_2(NMeH_2)_2]^{2+}$. It is known that pure GGAs tend to artificially lower the energy of low-spin states, whereas hybrid DFs are biased towards high-spin states. To validate the present DFT results, we calculated the singlet–quintet spin splittings of the recently characterized high-valent iron(VI) complex $[(Me_3cy\text{-}ac)FeN]^{2+}$ (Me$_3$cy-ac = *N*-methylated cy-ac; cy-ac = 1,4,8,11-tetraazacyclotetradecane-1-acetate)[29] and the experimentally well-documented isostructural *trans*-dioxo ruthenium(VI)[27,36] and osmium(VI)[37–39] complexes with saturated amine ligands using the pure GGA, PW91, and the hybrid DF, B3LYP. Consistent with the experimental findings, both PW91 and B3LYP calculations gave a d$^2$ singlet ground state for these three complexes, with PW91 always predicting larger singlet–quintet spin splittings than B3LYP by as much as about 1 eV (see Tables S37 and S45 in the Supporting Information). Why are the results of pure GGA and meta-GGA calculations on the *trans*-dioxo iron(VI) complex different from those of hybrid DF ones? A close look at the geometries of *trans*-$[Fe(O)_2(NH_3)_2(NMeH_2)_2]^{2+}$ optimized with different DFs indicated that both pure GGAs (PW91, BP86, and OLYP) and meta-GGAs (VSXC and HCTH407) gave a bent O-Fe-O angle in the quintet state (ca. 164–168°), whereas a linear O-Fe-O unit was found for the quintet geometries optimized with the hybrid DFs B3LYP and PBE1PBE (see Table 1). If we used B3LYP to calculate the singlet–quintet spin splitting of *trans*-$[Fe(O)_2(NH_3)_2(NMeH_2)_2]^{2+}$ on the PW91 optimized structure, the quintet state would be marginally higher in energy than the singlet state (the singlet–quintet splitting is ca. 0.03 eV). Indeed, similar bent angles along the X-M-Y axes (X, Y = axial ligands; M = Fe, Ru, Os) for $[(Me_3cy\text{-}ac)FeN]^{2+}$, *trans*-$[Ru(O)_2(NH_3)_2(NMeH_2)_2]^{2+}$, and *trans*-$[Os(O)_2(NH_3)_2(NMeH_2)_2]^{2+}$ were obtained from both PW91 and B3LYP quintet-state geometry optimizations (see Table S46 in the Supporting Information). It remains unclear why a linear O-

Table 1. Selected geometrical parameters (bond lengths [Å] and angles [°]) and relative energies ($E_{rel}$) of *trans*-$[Fe(O)_2(NH_3)_2(NMeH_2)_2]^{2+}$ in various optimized spin states *S* with different DFs.[a]

| DF | *S* | *r*(Fe–O) | | *r*(Fe–NH$_3$) | | *r*(Fe–NMeH$_2$) | | ∢(O-Fe-O) | $E_{rel}$ [eV][b] |
|---|---|---|---|---|---|---|---|---|---|
| PW91 | 0 | 1.614 | 1.613 | 2.059 | 2.059 | 2.095 | 2.095 | 180 | 0.00 (0.00) |
| | 1 | 1.670 | 1.667 | 2.025 | 2.039 | 2.078 | 2.139 | 166 | 0.87 (0.80) |
| | 2 | 1.740 | 1.736 | 2.016 | 2.054 | 2.051 | 2.107 | 164 | 1.18 (1.07) |
| BP86 | 0 | 1.615 | 1.614 | 2.065 | 2.065 | 2.102 | 2.102 | 180 | 0.00 (0.00) |
| | 1 | 1.671 | 1.670 | 2.033 | 2.042 | 2.085 | 2.143 | 166 | 0.88 (0.81) |
| | 2 | 1.742 | 1.737 | 2.021 | 2.060 | 2.055 | 2.114 | 164 | 1.22 (1.11) |
| OLYP | 0 | 1.612 | 1.607 | 2.091 | 2.091 | 2.143 | 2.143 | 180 | 0.00 (0.00) |
| | 1 | does not converge | | | | | | | |
| | 2 | 1.742 | 1.737 | 2.048 | 2.081 | 2.088 | 2.176 | 163 | 0.98 (0.88) |
| B3LYP | 0 | 1.595 | 1.592 | 2.059 | 2.059 | 2.088 | 2.088 | 180 | 0.00 (0.00) |
| | 1 | does not converge | | | | | | | |
| | 2 | 1.748 | 1.761 | 2.045 | 2.046 | 2.064 | 2.064 | 180 | −0.14 (−0.26) |
| PBE1PBE | 0 | 1.582 | 1.580 | 2.031 | 2.032 | 2.055 | 2.054 | 180 | 0.00 (0.00) |
| | 1 | 1.718 | 1.704 | 2.024 | 2.024 | 2.021 | 2.021 | 180 | −0.36 (−0.48) |
| | 2 | 1.744 | 1.754 | 2.015 | 2.015 | 2.029 | 2.029 | 180 | −0.46 (−0.58) |
| HCTH407 | 0 | 1.605 | 1.601 | 2.090 | 2.090 | 2.145 | 2.145 | 180 | 0.00 (0.00) |
| | 1 | does not converge | | | | | | | |
| | 2 | 1.737 | 1.735 | 2.048 | 2.085 | 2.102 | 2.165 | 164 | 0.87 (0.79) |
| VSXC | 0 | 1.612 | 1.624 | 2.060 | 2.055 | 2.086 | 2.081 | 179 | 0.00 (0.00) |
| | 1 | does not converge | | | | | | | |
| | 2 | 1.719 | 1.794 | 2.033 | 2.042 | 2.053 | 2.071 | 168 | 0.56 (0.45) |

[a] DF/6-31G* results. [b] The energy of the optimized singlet state is set to zero. The values in parentheses are the relative thermal Gibbs free energies.

Fe-O angle at the quintet state of *trans*-$[Fe(O)_2(NH_3)_2(NMeH_2)_2]^{2+}$ was predicted by the B3LYP and PBE1PBE hybrid DFs. Because we have not been able to resolve the ground state of *trans*-$[Fe(O)_2(NH_3)_2(NMeH_2)_2]^{2+}$ to be a singlet or a quintet, herein we will discuss the electronic structures, spectroscopic properties, and redox potentials of *trans*-$[Fe(O)_2(NH_3)_2(NMeH_2)_2]^{2+}$ for both PW91 and B3LYP calculations.[40] For *trans*-$[M(O)_2(NH_3)_2(NMeH_2)_2]^{2+}$ complexes with M = Ru and Os, only the PW91 results are given because both PW91 and B3LYP calculations were found to give similar results. The calculations on $[M(O)_2(NH_3)_2(NMeH_2)_2]^{2+}$ (M = Ru and Os) will be compared with the literature data of *trans*-dioxo ruthenium(VI) and osmium(VI) complexes with saturated amine ligands.

**Electronic structure of *trans*-$[M(O)_2(NH_3)_2(NMeH_2)_2]^{2+}$**: The ground-state geometrical parameters, vibrational frequencies of the symmetric ($\nu_{sym}$) and asymmetric ($\nu_{asym}$) vibrational modes of the O-M-O unit, and the force constants of the M–O bond ($k_{M-O}$) from PW91 computations are listed in Table 2. The calculated M–O distances of 1.736 and 1.760 Å on average for M = Ru and Os, respectively, are slightly longer than the corresponding X-ray data (Ru–O 1.718(5) and 1.705(7) Å in *trans*-$[Ru^{VI}(15\text{-TMC})(O)_2](ClO_4)_2$ and *trans*-$[Ru^{VI}(16\text{-TMC})(O)_2](ClO_4)_2$, respectively,[27] and Os–O 1.735(6) Å in *trans*-$[Os^{VI}(14\text{-TMC})(O)_2](PF_6)_2$;[37] 14-TMC = 1,4,8,11-tetramethyl-1,4,8,11-tetraazacyclotetradecane, 15-TMC = 1,4,8,12-tetramethyl-1,4,8,12-tetraazacyclopentadecane, 16-TMC = 1,5,9,13-tetramethyl-1,5,9,13-tetraazacyclohexadecane), but comparable to the results of the recent DFT studies on *trans*-$[M^{VI}(O)_2(NH_3)_4]^{2+}$ by Gray and co-workers (Ru–O 1.724–1.752, Os–O 1.752–1.777).[33] The largest difference between the calculated and experimental distances is about 0.033 Å for the Ru–O bond, which is a typical accuracy for metal–ligand multiple bonds from DFT calculations.[41] The computed Ru–$N_{amine}$ distances are 2.176–2.197 Å, which are comparable to those found in the crystal structures of *trans*-$[Ru(15\text{-TMC})(O)_2](ClO_4)_2$ and *trans*-$[Ru(16\text{-TMC})(O)_2](ClO_4)_2$ (2.17(1)-2.24(1) Å).[27] However, the calculated Os–$N_{amine}$ distances are longer by as much as 0.076 Å when compared with those in *trans*-$[Os^{VI}(14\text{-TMC})(O)_2](PF_6)_2$.[37] Similar M–$N_{amine}$ distances to those from our DFT studies were also obtained by Gray and co-workers (2.152–2.182 Å for Ru–$N_{amine}$ and 2.164–2.193 Å for Os–$N_{amine}$ in *trans*-$[M^{VI}(O)_2(NH_3)_4]^{2+}$).[33]

From PW91 optimizations, the calculated Fe–O bond length for the ground state of *trans*-$[Fe(O)_2(NH_3)_2(NMeH_2)_2]^{2+}$ is about 1.613 Å, which is shorter than that in $K_2Fe^{VI}O_4$ (1.666(2) Å on average)[18] and the reported $Fe^{IV}$=O distances of 1.639(5) and 1.646(3) Å for $[Fe^{IV}(O)(N4Py)]^{2+}$ and $[Fe^{IV}(O)(14\text{-TMC})(NCCH_3)](SO_3CF_3)_2$, respectively (N4Py = *N*,*N*-bis(2-pyridylmethyl)-*N*-bis(2-pyridyl)methylamine).[9,12] This is consistent with the bonding picture that, in the tetrahedral $d^2$ $Fe^{VI}O_4{}^{2-}$ anion, the two d electrons reside in the Fe–O antibonding e orbitals[21] and in the non-heme $d^4$ $Fe^{IV}$=O complexes, two of the d electrons go to the Fe–O π-antibonding orbitals $[Fe(d_\pi)-O(p_\pi{}^*)]$, whereas the other two d electrons occupy the nonbonding $Fe(d_{xy})$ orbitals.[42] On the other hand, the PW91 calculated ground state of *trans*-$[Fe(O)_2(NH_3)_2(NMeH_2)_2]^{2+}$ has a $d^2$ electronic configuration in which the two d electrons reside in the nonbonding $Fe(d_{xy})$ orbitals (see below). The Fe–$N_{amine}$ distances were calculated to be 2.059–2.095 Å, comparable to the Fe–$N_{14\text{-TMC}}$ distances of 2.067(3)–2.117(3) Å found in $[Fe^{IV}(O)(14\text{-TMC})(NCCH_3)](SO_3CF_3)_2$[9] as well as the Fe–$N_{amine}$ distances of 2.05–2.07 Å obtained from DFT calculations on $[Fe(O)(L)_4(NCCH_3)]^{2+}$ (L = $NH_3$, $NMeH_2$).[42] Because the 14-TMC ligand is not involved in Fe–O π-antibonding orbitals,[42] removal of two electrons from these antibonding orbitals, which are composed solely of $Fe(d_\pi)$ and $O(p_\pi)$, that is, oxidation of oxo iron(IV) to oxo iron(VI), would not result in a significant change in Fe–$N_{amine}$ distances. Similar Ru–$N_{amine}$ distances in both $Ru^{IV}$ and $Ru^{VI}$ oxo complexes with macrocyclic tertiary amine ligands were previously reported.[27] In general, the M–O and M–$N_{amine}$ distances increase down the group. The increase is more pronounced from Fe to Ru than from Ru to Os (more than 0.12 Å in the former, but less than 0.03 Å in the latter case), which is a consequence of shell-size expansion versus relativistic contraction when one goes from second- to third-row transition metals.[43] The O-M-O angles of the ground states obtained from PW91 calculations are linear in all cases, which is consistent with X-ray data.[27,37]

Table 2. Optimized ground state geometrical parameters (bond lengths [Å] and angles [°]), vibrational frequencies ($\tilde{\nu}$), and force constants ($k_{M-O}$) for *trans*-$[M(O)_2(NH_3)_2(NMeH_2)_2]^{2+}$ (M = Fe, Ru, Os) from PW91 calculations.[a]

| M | $r(M{=}O)$ | $r(M-N_{amine})$ | $\sphericalangle$(O-M-O) | $\tilde{\nu}_{asym}$(O-M-O) | $\tilde{\nu}_{sym}$(O-M-O) | $k_{M-O}$ [N m$^{-1}$] |
|---|---|---|---|---|---|---|
| $Fe^{VI}$ | 1.613 (1.748)<br>1.614 (1.761) | 2.059 (2.045)<br>2.095 (2.064)<br>2.059 (2.046)<br>2.095 (2.063) | 180 (180) | 965 (533) | 857 (656) | 626.2 (263) |
| $Ru^{VI}$ | 1.734<br>1.738 | 2.176<br>2.197<br>2.178<br>2.196 | 179 | 914 | 877 | 662.3 |
| $Os^{VI}$ | 1.762<br>1.758 | 2.182<br>2.203<br>2.182<br>2.203 | 180 | 906 | 920 | 729.1 |

[a] The values in parentheses are from B3LYP calculations on the quintet state (the lowest energy state from B3LYP calculations).

From B3LYP optimizations, the ground state of *trans*-$[Fe(O)_2(NH_3)_2(NMeH_2)_2]^{2+}$ is a quintet with Fe–O distances of 1.748 and 1.761 Å, which are longer than those of ferrate(VI) and iron(IV) oxo (less than 1.67 Å, see above) by more than 0.07 Å. This is because in the B3LYP optimized quintet state of *trans*-$[Fe(O)_2(NH_3)_2(NMeH_2)_2]^{2+}$ 1) there are two unpaired electrons in the Fe−O π antibonding orbitals, as in the case of iron(IV) oxo complexes; and 2) the Fe−O π bonding orbitals (see Figure 1 for MOs) are each singly occupied, whereas the analogous Fe−O π-bonding orbitals are doubly occupied in the ground states of both ferrate(VI) and iron(IV) oxo complexes. Because the Fe−O π-bonding and antibonding orbitals are not quasidegenerate or close-lying, the energy gain in an electronic structure with Fe−O π-bonding and antibonding orbitals in parallel spins (by Hund's rule) in *trans*-$[Fe(O)_2(NH_3)_2(NMeH_2)_2]^{2+}$ (the quintet state) should not be large enough to override the energy penalty of promoting two electrons from the π(Fe−O) bonding orbital, which is fully filled, in its singlet state to empty π*(Fe−O) antibonding orbitals.

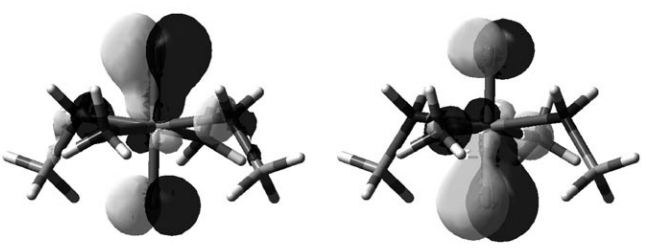

Figure 1. Two of the MO surfaces of the singly occupied orbitals of *trans*-$[Fe(O)_2(NH_3)_2(NMeH_2)_2]^{2+}$ in the B3LYP optimized quintet state (isovalue = 0.05 a.u.).

The calculated frequencies of the asymmetric ($\nu_{asym}$) and symmetric vibrational ($\nu_{sym}$) modes for *trans*-$[Os(O)_2(NH_3)_2(NMeH_2)_2]^{2+}$ in its singlet ground state are 906 and 920 cm$^{-1}$, respectively. These values are slightly higher than the experimental data of 875 ($\nu_{asym}$) and 917 cm$^{-1}$ ($\nu_{sym}$) obtained.[39,44] For *trans*-$[Ru(O)_2(NH_3)_2(NMeH_2)_2]^{2+}$, the $\nu_{asym}$ and $\nu_{sym}$ stretching vibrations are calculated to be 914 and 877 cm$^{-1}$, respectively, which are higher than the experimental values of 840–860 ($\nu_{asym}$) and approximately 820 cm$^{-1}$ ($\nu_{sym}$) by more than 50 cm$^{-1}$.[45,46] The O-Fe-O asymmetric and symmetric stretching frequencies from PW91 calculations were calculated to be 965 and 857 cm$^{-1}$, respectively, with the former value higher than the $Fe^{IV}$=O stretching frequency of 834 cm$^{-1}$ in $[Fe^{IV}(O)(14\text{-}TMC)(NCCH_3)](SO_3CF_3)_2$.[9] Similar behavior could be found in the related ruthenium oxo complexes: $\nu_{asym}$(O-Ru-O) = 840–860 cm$^{-1}$ for the *trans*-dioxo ruthenium(VI) complexes, which are higher than the $Ru^{IV}$=O stretching frequencies of 815–820 and 792 cm$^{-1}$ in oxo ruthenium(IV) complexes supported by macrocyclic N-donor[27] and polypyridyl[47] ligands, respectively. The O-Fe-O asymmetric vibration is at a higher frequency than its symmetric counterpart, similar in magnitude, and consistent with the trend of O-M-O stretching frequencies of other linear 3d transition metal dioxides ($CoO_2$: 954 ($\nu_{asym}$) and 772 cm$^{-1}$ ($\nu_{sym}$); $NiO_2$: 955 ($\nu_{asym}$) and 750 cm$^{-1}$ ($\nu_{sym}$)).[48] In the B3LYP optimized quintet state, the O-Fe-O asymmetric and symmetric stretching frequencies drop to 656 and 533 cm$^{-1}$, respectively, owing to lengthening of the Fe−O bond.

To obtain a quantitative description of the M−O bond, normal coordinate calculations were carried out on the linear O=M=O moieties, and the force constants ($k_{M-O}$) are listed in Table 2. The calculated force constants are in the order Fe < Ru < Os (irrespective of whether the ground state for M=Fe is a singlet or a quintet from PW91 and B3LYP optimizations, respectively), that is, the Os−O bond is the strongest and the Fe−O bond the weakest.

Atomic-charge analysis can give information about the interactions between the metal ion and axial oxo ligands. Table 3 presents the NBO analysis of the *trans*-$[M(O)_2(NH_3)_2(NMeH_2)_2]^{2+}$ complexes (M = Fe, Ru, and Os) in the PW91 optimized singlet states. The NBO charges of the metal ions are all less than +6, that is, the interactions between M and O atoms are covalent. In addition, as the NBO charges for both M and O in *trans*-$[M(O)_2(NH_3)_2(NMeH_2)_2]^{2+}$ increase down the group, the M−O bonds of *trans*-dioxo iron(VI) have the highest covalency. This is also revealed by the electronic populations of the $d_{xz}$, $d_{yz}$, and $d_{z^2}$ orbitals by NBO analyses (also listed in Table 3). Based on the data in Table 3, both π and σ donations from the oxo ligands occur. Because the electronic populations of these d orbitals are in the order Fe > Ru > Os, the covalent interaction between the metal ion and oxo ligands also follows the same order (Fe > Ru > Os), in accordance with the expectation that $Fe^{VI}$ should have the highest electron affinity when compared with $Ru^{VI}$ and $Os^{VI}$.

Table 3. NBO charges and d-orbital electronic populations in *trans*-$[M(O)_2(NH_3)_2(NMeH_2)_2]^{2+}$ (M = Fe, Ru, Os) in the PW91 optimized ground-state geometries.

| | Fe | Ru | Os |
|---|---|---|---|
| M | +0.84 | +1.01 | +1.23 |
| $d_{xz}$ | 1.26e | 1.21e | 1.19e |
| $d_{yz}$ | 1.26e | 1.20e | 1.13e |
| $d_{z^2}$ | 1.18e | 1.09e | 1.03e |
| O | −0.24 | −0.32 | −0.39 |
| | −0.22 | −0.30 | −0.41 |
| amine ligands | +1.62 | +1.61 | +1.57 |

Orbital descriptions are useful in understanding spectroscopic behavior and reactivity. The orbital energies and atomic compositions of the frontier molecular orbitals (FMOs) of *trans*-$[M(O)_2(NH_3)_2(NMeH_2)_2]^{2+}$ with M = Fe, Ru, and Os from PW91 computations are listed in Tables 4 to 6, and the MO diagram is depicted in Figure 2. In a distorted octahedral environment with strong axial metal–oxo interactions, the lowest lying d orbital is M($d_{xy}$), followed by an almost doubly degenerate pair of π-antibonding combinations of M($d_\pi$) and O($p_\pi$*) orbitals. The highest energy d orbital results from a σ-antibonding combination of M($d_{z^2}$) and $N_{amine}$($p_\sigma$) orbitals. In addition, two low-lying nonbonding orbitals are composed of O($p_\pi$) and $N_{amine}$($p_\sigma$*) orbitals

Table 4. Orbital energies and atomic contributions of the FMOs of *trans*-$[Fe(O)_2(NH_3)_2(NMeH_2)_2]^{2+}$ in the PW91 optimized ground state structure.

| MO | Energy [eV] | Fe [%] | O16 [%] | O17 [%] | $NMeH_2$ [%] | $NH_3$ [%] |
|---|---|---|---|---|---|---|
| HOMO−4 | −9.14 | 7 | 19 | 21 | 52 | 0 |
| HOMO−3 | −8.85 | 3 | 49 | 47 | 1 | 0 |
| HOMO−2 | −8.30 | 95 | 0 | 0 | 3 | 2 |
| HOMO−1 | −8.07 | 1 | 35 | 35 | 1 | 28 |
| HOMO | −7.91 | 1 | 21 | 22 | 56 | 0 |
| LUMO | −6.32 | 47 | 26 | 27 | 0 | 0 |
| LUMO+1 | −6.27 | 47 | 26 | 26 | 1 | 0 |
| LUMO+2 | −5.15 | 53 | 0 | 0 | 26 | 21 |
| LUMO+3 | −3.54 | 49 | 15 | 15 | 12 | 9 |

Table 5. Orbital energies and atomic contributions of the FMOs of *trans*-$[Ru(O)_2(NH_3)_2(NMeH_2)_2]^{2+}$ in the PW91 optimized ground-state structure.

| MO | Energy [eV] | Ru [%] | O16 [%] | O17 [%] | $NMeH_2$ [%] | $NH_3$ [%] |
|---|---|---|---|---|---|---|
| HOMO−4 | −9.00 | 6 | 23 | 24 | 47 | 0 |
| HOMO−3 | −8.47 | 4 | 48 | 47 | 0 | 0 |
| HOMO−2 | −8.36 | 2 | 36 | 36 | 0 | 26 |
| HOMO−1 | −8.18 | 3 | 21 | 20 | 56 | 0 |
| HOMO | −8.02 | 90 | 1 | 1 | 6 | 3 |
| LUMO | −5.52 | 48 | 26 | 26 | 0 | 0 |
| LUMO+1 | −5.48 | 48 | 26 | 26 | 1 | 0 |
| LUMO+2 | −4.03 | 53 | 0 | 0 | 25 | 22 |
| LUMO+3 | −1.81 | 60 | 8 | 8 | 13 | 11 |

Table 6. Orbital energies and atomic contributions [%] of the FMOs of *trans*-$[Os(O)_2(NH_3)_2(NMeH_2)_2]^{2+}$ in the PW91 optimized ground-state structure.

| MO | Energy [eV] | Os [%] | O16 [%] | O17 [%] | $NMeH_2$ [%] | $NH_3$ [%] |
|---|---|---|---|---|---|---|
| HOMO−4 | −9.01 | 6 | 16 | 15 | 63 | 0 |
| HOMO−3 | −8.36 | 4 | 47 | 49 | 0 | 0 |
| HOMO−2 | −8.35 | 2 | 39 | 40 | 0 | 19 |
| HOMO−1 | −8.23 | 1 | 28 | 30 | 41 | 0 |
| HOMO | −7.64 | 91 | 0 | 0 | 5 | 4 |
| LUMO | −4.86 | 50 | 25 | 25 | 0 | 0 |
| LUMO+1 | −4.82 | 50 | 25 | 24 | 1 | 0 |
| LUMO+2 | −3.14 | 58 | 0 | 0 | 23 | 19 |
| LUMO+3 | −1.59 | 67 | 1 | 2 | 16 | 14 |

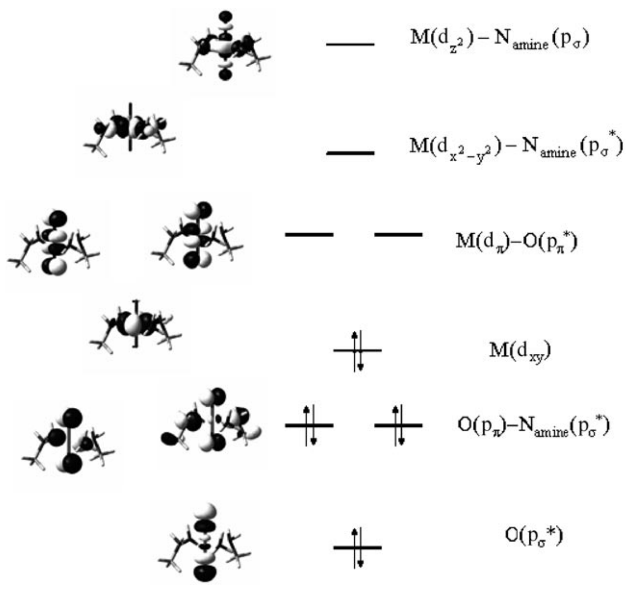

Figure 2. MO diagram of *trans*-$[M(O)_2(NH_3)_2(NMeH_2)_2]^{2+}$ (M = Fe, Ru, Os). Note that for M = Fe, the $M(d_{xy})$ and $O(p_\pi)$–$N_{amine}(p_\sigma^*)$ orbitals switch in order (see text).

along the *x* and *y* axes and one nonbonding orbital that is of $O(p_\sigma^*)$ character (see Figure 2).

Essentially, the present PW91 calculations, as well as other pure GGA and meta-GGA calculations performed in this work, predict a $d^2$ ground state electronic configuration, with only the $M(d_{xy})$ orbital doubly occupied (see Figure 2), so that the $M^{VI}$ oxidation state is an appropriate formalism for *trans*-$[M(O)_2(NH_3)_2(NMeH_2)_2]^{2+}$ complexes. With the exception of *trans*-$[Fe(O)_2(NH_3)_2(NMeH_2)_2]^{2+}$, $M(d_{xy})$ is the HOMO and the orbital energy increases down the group due to increasing energy of the d valence shell. For *trans*-$[Fe(O)_2(NH_3)_2(NMeH_2)_2]^{2+}$, $Fe(d_{xy})$ is the HOMO−2 orbital, whereas the nonbonding $O(p_\pi)$–$N_{amine}(p_\sigma^*)$ orbitals are the HOMO and HOMO−1 orbitals. On the other hand, for *trans*-$[M(O)_2(NH_3)_2(NMeH_2)_2]^{2+}$ (M = Ru and Os), these nonbonding orbitals correspond to the HOMO−1 and HOMO−2 orbitals. The metal–oxo bonds are formed by σ overlap between the $M(d_{z^2})$ and $p_\sigma$ orbitals of both $N_{amine}$ and O atoms (MO30, MO32, and MO31 for M = Fe, Ru, and Os, respectively; for orbital diagrams, see Tables S47–S49 in the Supporting Information) and π overlap between $M(d_\pi)$ and $O(p_\pi^*)$ orbitals with the electron density delocalized over M and the two oxygen atoms (MO33 and MO34, see Tables S47–S49 in the Supporting Information). The corresponding σ- and π-antibonding orbitals are LUMO+3 and LUMO/LUMO+1 orbitals, respectively. The σ M−O bonding orbitals are dominated by ligand functions (see Tables S47–S49 in the Supporting Information); which is reflected in the greater metal character in the corresponding σ* orbitals (LUMO+3, see Tables 3–5 for atomic contributions). The M−O π bonds have an appreciable contribution from the $M(d_\pi)$ orbitals, with metal character in the order Fe (45–47 %) > Ru (37–44 %) ≈ Os (36–42 %). This indicates strong mixing between $M(d_\pi)$ and $O(p_\pi)$ orbitals, which imparts covalency on the M−O bond and decreases the effective cationic charge on M, in agreement with the NBO analyses discussed above (all of the metal atoms have NBO charges less than +6, of which Fe is the least positive and Os is the most positive). As the metal character in both σ and π M−O bonds decreases from Fe to Ru to Os, charge transfer from the oxo ligands to the metal ion should be the least for Os and the most for Fe. Hence, the Fe−O bond has the strongest covalency and the decrease in effective cationic charge resulting from Fe−O bond covalency may contribute to stabilization of *trans*-$[Fe(O)_2(NH_3)_2(NMeH_2)_2]^{2+}$.

**Spectroscopic properties**: Time-dependent DFT (TDDFT) calculations with the PW91 DF were employed to examine the spectroscopic properties of *trans*-$[M(O)_2(NH_3)_2(NMeH_2)_2]^{2+}$ complexes (M = Fe, Ru, and Os) in their optimized singlet ground-state geometries with solvent approximated as a dielectric medium by using the conductor-like polarizable continuum model (CPCM). For M = Fe, the transition energies were also computed for the B3LYP optimized quintet ground-state geometry. For M = Ru and Os, the calculated excitation energies were compared with experimental UV/Vis absorption spectra of *trans*-$[M(O)_2L]^{2+}$ (M = Ru and Os; L = 14-TMC, 15-TMC, and 16-TMC). The simulated absorption spectra for *trans*-$[M(O)_2(NH_3)_2(NMeH_2)_2]^{2+}$ (M = Fe, Ru, and Os) in water are shown in Figure 3. Selected calculated transition energies contributing to the observed bands in the simulated absorption spectra (bands I and II, see Figure 3) are listed in Table 7. For a complete list of the TDDFT results, see Tables S50–S52 in the Supporting Information. Note that singlet–triplet transitions were not included in the spectral simulations because spin–orbit coupling was not explicitly included in the TDDFT calculations.

The simulated spectra reveal a broad band (band I) at about 510, 380, and 300–330 nm for M = Fe, Ru, and Os, respectively, and the intensity of this band increases down the group. Examination of the calculated electronic transitions contributing to band I revealed that, with the exception of M = Fe, this band is comprised of two types of transitions: the higher energy band IA ($\lambda = 363$ and 300 nm for Ru and Os, respectively), arises from HOMO−4→LUMO+1 and HOMO−2→LUMO transitions, in which both HOMO−4 and HOMO−2 are nonbonding orbitals composed of $O(p_\pi)$ and $N_{amine}(p_\sigma{}^*)$ orbitals (see Figure 2 and Tables S47–S49 in the Supporting Information for orbital diagrams); the lower energy band IB ($\lambda = 388$ and 384 nm for Ru and $\lambda = 333$ and 329 nm for Os), is derived from HOMO−3 $[O(p_\sigma{}^*)]\rightarrow$ LUMO and HOMO−3 $[O(p_\sigma{}^*)]\rightarrow$LUMO+1 $[M(d_\pi)\text{–}O(p_\pi{}^*)]$ transitions. Bands IA and IB are both of ligand-to-metal charge-transfer (LMCT) nature. The energies of bands IA and IB compare well with those of the experimental absorption bands at $\lambda_{max} \approx 375\text{–}390$ nm for *trans*-$[Ru^{VI}O_2(L)]^{2+}$ (L = 14-TMC, 15-TMC, 16-TMC, or $(NH_3)_4$)[27,36] and $\lambda_{max} \approx 300\text{–}315$ nm for *trans*-$[Os(O)_2(L)]^{2+}$ (L = 14-TMC, 15-TMC, and 16-TMC),[38,39] both of which have previously been assigned as $^1[O(p_\pi)\text{–}M(d_\pi)]$ LMCT transitions.[49,50] Weak absorptions with $\varepsilon \approx 10^2\,dm^3mol^{-1}cm^{-1}$ were also observed at $\lambda \approx 350\text{–}370$ nm in the UV/Vis absorption spectra of *trans*-$[Os^{VI}O_2(L)]^{2+}$ (L = 14-TMC, 15-TMC, and 16-TMC)[38,39] and were previously assigned as $^3[O(p_\pi)\text{–}Os(d_\pi)]$ LMCT transitions.[49] As our TDDFT calculations did not take spin–orbit coupling into account, all spin-forbidden transitions have zero oscillator strength, and only spin-allowed singlet transitions are considered in the spectral simulations depicted in Figure 3. The calculated singlet–triplet transition energies for $^3[O(p_\pi)\text{–}N_{amine}(p_\sigma{}^*)\rightarrow Os(d_\pi)\text{–}O(p_\pi{}^*)]$ and $^3[O(p_\sigma{}^*)\rightarrow Os(d_\pi)\text{–}O(p_\pi{}^*)]$ are about 310 and 395–400 nm, respectively. Another $^3$LMCT transition calculated at about 360 nm is derived from HOMO−2→LUMO and HOMO−1→LUMO+1 transitions and is $^3[O(p_\pi)\text{–}N_{amine}(p_\sigma{}^*)\rightarrow Os(d_\pi)\text{–}O(p_\pi{}^*)]$ in nature.

In the case of M = Fe, band I at about 510 nm is attributed to HOMO−4→LUMO+1 and HOMO−1→LUMO transitions, similar in nature to band IA $^1[O(p_\pi)\text{–}N_{amine}(p_\sigma{}^*)\rightarrow M(d_\pi)\text{–}O(p_\pi{}^*)]$ discussed above for M = Ru and Os. The cor-

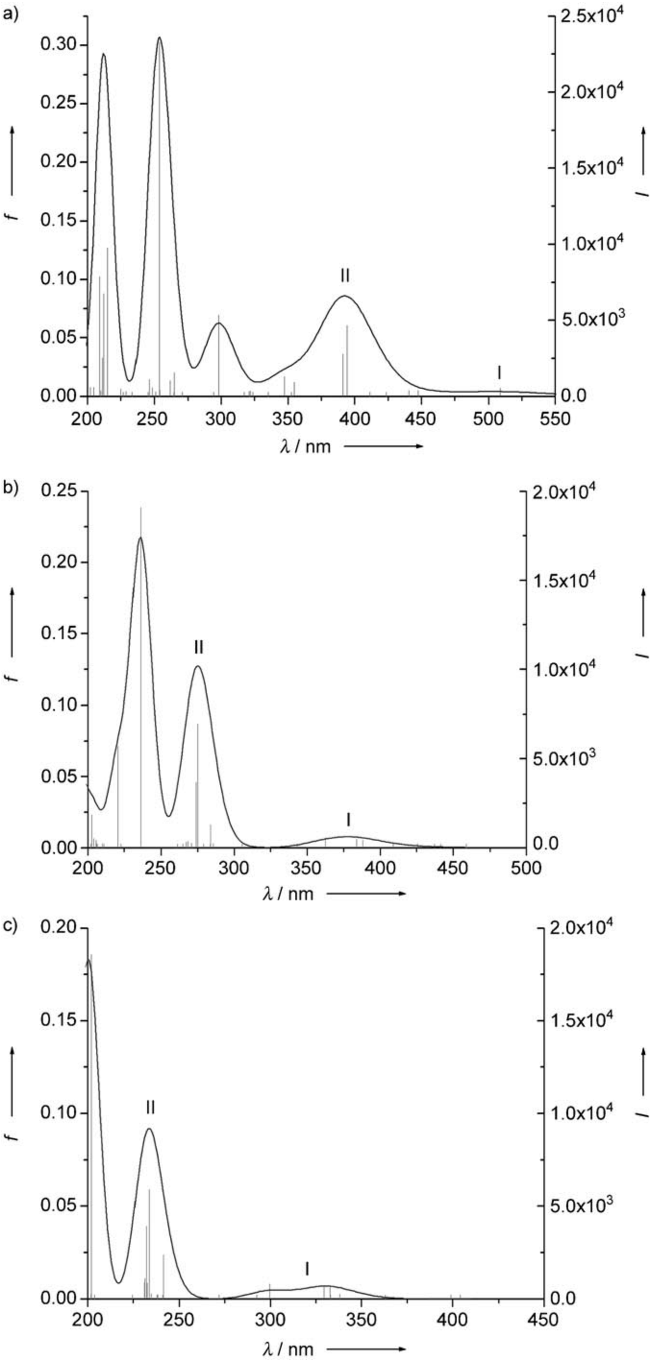

Figure 3. Simulated absorption spectra in water at the PW91 optimized singlet-state geometry for a) *trans*-$[Fe^{VI}(O)_2(NH_3)_2(NMeH_2)_2]^{2+}$, b) *trans*-$[Ru^{VI}(O)_2(NH_3)_2(NMeH_2)_2]^{2+}$, and c) *trans*-$[Os^{VI}(O)_2(NH_3)_2(NMeH_2)_2]^{2+}$. The vertical lines are individual electronic transitions.

Table 7. Selected calculated transition energies ($\lambda$) and oscillator strengths ($f$) of *trans*-$[M(O)_2(NH_3)_2(NMeH_2)_2]^{2+}$ (M = Fe, Ru, Os) by TDDFT/CPCM in the PW91 optimized singlet ground-state geometries in water. Major contributions are shown along with the nature of the transitions.

| M | $\lambda$ [nm] | $f$ | Major contributions[a] | Nature of transition | Band |
|---|---|---|---|---|---|
| Fe | 509 | 0.0038 | HOMO−4→LUMO+1 (−0.39)<br>HOMO−1→LUMO (0.46) | $O(p_\pi)–N_{amine}(p_\sigma*)\rightarrow Fe(d_\pi)–O(p_\pi*)$ | I |
|  | 447 | 0.0016 | HOMO−3→LUMO (0.67) | $O(p_\sigma*)\rightarrow Fe(d_\pi)$ |  |
|  | 441 | 0.0017 | HOMO−3→LUMO+1 (0.69) | $O(p_\sigma*)\rightarrow Fe(d_\pi)$ |  |
|  | 394 | 0.0572 | HOMO→LUMO+2 (0.62) | $O(p_\pi)–N_{amine}(p_\sigma*)\rightarrow N_{amine}(p_\sigma*)–Fe(d_{x^2-y^2})$ | II |
|  | 391 | 0.027 | HOMO−1→LUMO+2 (0.66) | $O(p_\pi)–N_{amine}(p_\sigma*)\rightarrow N_{amine}(p_\sigma*)–M(d_{x^2-y^2})$ | II |
| Ru | 388 | 0.0029 | HOMO−3→LUMO (0.68) | $O(p_\sigma*)\rightarrow Ru(d_\pi)$ | I |
|  | 384 | 0.0033 | HOMO−3→LUMO+1 (0.68) | $O(p_\sigma*)\rightarrow Ru(d_\pi)$ | I |
|  | 363 | 0.0042 | HOMO−4→LUMO+1 (−0.46)<br>HOMO−2→LUMO (0.47) | $O(p_\pi)–N_{amine}(p_\sigma*)\rightarrow Ru(d_\pi)–O(p_\pi*)$ | I |
|  | 275 | 0.0846 | HOMO−1→LUMO+2 (0.60) | $O(p_\pi)–N_{amine}(p_\sigma*)\rightarrow N_{amine}(p_\sigma*)\text{-}Ru(d_{x^2-y^2})$ | II |
|  | 274 | 0.0434 | HOMO−2→LUMO+2 (0.68) | $O(p_\pi)–N_{amine}(p_\sigma*)\rightarrow N_{amine}(p_\sigma*)–Ru(d_{x^2-y^2})$ | II |
| Os | 333 | 0.0041 | HOMO−3→LUMO (0.68) | $O(p_\sigma*)\rightarrow Os(d_\pi)$ | I |
|  | 329 | 0.0047 | HOMO−3→LUMO+1 (0.68) | $O(p_\sigma*)\rightarrow Os(d_\pi)$ | I |
|  | 300 | 0.0060 | HOMO−4→LUMO+1 (0.56)<br>HOMO−2→LUMO (-0.38) | $O(p_\pi)–N_{amine}(p_\sigma*)\rightarrow Os(d_\pi)–O(p_\pi*)$ | I |
|  | 234 | 0.0570 | HOMO−1→LUMO+2 (0.61) | $O(p_\pi)–N_{amine}(p_\sigma*)\rightarrow N_{amine}(p_\sigma*)–Os(d_{x^2-y^2})$ | II |
|  | 232 | 0.0372 | HOMO−2→LUMO+2 (0.68) | $O(p_\pi)–N_{amine}(p_\sigma*)\rightarrow N_{amine}(p_\sigma*)\text{-}Os(d_{x^2-y^2})$ | II |

[a] CI coefficients in parentheses.

responding band IB (HOMO−3→LUMO and LUMO+1; $O(p_\sigma*)\rightarrow M(d_\pi)$ at $\lambda \approx 447$ and 441 nm) for *trans*-$[Fe(O)_2(NH_3)_2(NMeH_2)_2]^{2+}$ is masked by the stronger band II when each electronic transition is simulated as a Gaussian peak with a full width at half maximum (fwhm) of 3000 cm$^{-1}$. There is a substantial shift in the absorption energy of band I when one goes from Os to Fe: about 14000 cm$^{-1}$ (ca. 1.7 eV) for band IA $[O(p_\pi)–N_{amine}(p_\sigma*)\rightarrow M(d_\pi)–O(p_\pi*)]$ and about 8000 cm$^{-1}$ (ca. 1.0 eV) for band IB $[O(p_\sigma*)\rightarrow M(d_\pi)]$. This large shift is due to the fact that HOMO−3, HOMO−4, and HOMO−2 (HOMO−1 for M = Fe) are nonbonding in nature and are composed mainly of oxo and amine ligand functions, and hence, their energies change only slightly among Fe, Ru, and Os. However, the LUMO and LUMO+1 are M−O π* orbitals, which become more high lying as one goes down the group, since the d-valence shell energy increases from 3d to 4d to 5d. Hence, the LUMO and LUMO+1 orbitals increase in energy from Fe to Ru to Os, and this leads to a blueshift of both bands IA and IB from Fe to Os (see Tables 3–5 for orbital energies). When M = Fe, the lowest energy spin-allowed singlet absorption band is not the $O(p_\sigma*)\rightarrow Fe(d_\pi)$ transition, as is the case of M = Ru and Os, but the $O(p_\pi)–N_{amine}(p_\sigma*)\rightarrow M(d_\pi)–O(p_\pi*)$ transition.

The next lower energy bands (band II) of *trans*-$[M(O)_2(NH_3)_2(NMeH_2)_2]^{2+}$ are calculated at about 392, 274, and 233 nm for M = Fe, Ru, and Os respectively. This band is derived from HOMO−1 and HOMO−2 (for Fe, HOMO and HOMO−1)→LUMO+2 transitions. The occupied orbitals are nonbonding in nature and are of $O(p_\pi)–N_{amine}(p_\sigma*)$ character, whereas the LUMO+2 orbital is a σ-antibonding combination of $N_{amine}(p_\sigma*)$ and $M(d_{x^2-y^2})$ orbitals. Thus, this band is described as an $O(p_\pi)–N_{amine}(p_\sigma*)\rightarrow N_{amine}(p_\sigma*)–M(d_{x^2-y^2})$ transition. Intense absorption bands for *trans*-$[M(O)_2L]^{2+}$ with M = Ru[27] and Os[38,39] (L = 14-TMC, 15-TMC, and 16-TMC) with $\lambda_{max}$ at about 250–310 and 260 nm, respectively, have previously been reported, and these absorption bands may correspond to the calculated band II in the present work. We previously reported that for *trans*-$[Ru(O)_2L]^{2+}$ (L = 14-TMC, 15-TMC, and 16-TMC) variation of the position and relative extinction coefficients of the two intense absorption bands at about 220–260 and 250–310 nm with the ring size of the tetraaza macrocycle suggests involvement of $N_{amine}$ character in these transitions.[27] Our present assignment of band II to an $O(p_\pi)–N_{amine}(p_\sigma*)\rightarrow N_{amine}(p_\sigma*)–M(d_{x^2-y^2})$ transition is consistent with such an effect of the macrocycle ring size,[27] since the LUMO+2 orbital involves antibonding interactions between M and $N_{amine}$ with substantial $N_{amine}(p_\sigma)$ character (>40%).[51] Band II shows a significant blueshift in absorption energy by about 17000 cm$^{-1}$ (ca. 2.2 eV) from Fe to Os. This is because the excitation is from a nonbonding ligand MO (HOMO−1 and HOMO−2 for M = Ru and Os, and HOMO−1 and HOMO for M = Fe) to a σ-antibonding orbital (LUMO+2) that is mainly composed of $M(d_{x^2-y^2})$ and $N_{amine}(p_\sigma*)$ orbitals. As the compositions of the LUMO+2 orbitals for M = Fe, Ru, and Os are similar, the increase in LUMO+2 orbital energy is attributed to the increase in orbital energy of the d valence shell: 3d < 4d < 5d.

Because the hybrid B3LYP and PBE1PBE DFs predicted a quintet ground state for *trans*-$[Fe(O)_2(NH_3)_2(NMeH_2)_2]^{2+}$, we also computed the electronic transition energies in the B3LYP quintet-state optimized geometry by TD-B3LYP. The transition energies with $f > 0$ are given in Table 8.[52]

The three lowest intense transitions (with $f > 0.01$) for *trans*-$[Fe(O)_2(NH_3)_2(NMeH_2)]^{2+}$ at the B3LYP optimized quintet state geometry are at 515, 429, and 378 nm. These three absorption peak maxima are similar to those obtained from TD-PW91 calculations at the PW91 optimized singlet-state geometry ($\lambda = 509$, 394, and 391 nm), except for the peak maximum at 515 nm in the B3LYP optimized quintet state, which is predominantly a π→π* (Fe−O bond) transition (the 509 nm peak in the PW91 optimized singlet state is an LMCT transition). The absorption peaks at 429 and 378 nm are both of LMCT character. This is similar to the assignment of the 394 and 391 nm absorption peaks obtained in the PW91 optimized singlet-state geometry, though the orbital characters contributing to these two transitions are not the same in the two different DFT calculations. The weaker transitions ($f > 0.001$) with peak maxima at 462, 447, and 440 nm obtained from TD-B3LYP calculations on the

Table 8. Selected transition energies ($\lambda$) and oscillator strengths ($f$) of *trans*-$[\mathrm{Fe(O)_2(NH_3)_2(NMeH_2)_2}]^{2+}$ calculated by TDDFT/CPCM in the B3LYP optimized quintet ground-state geometries in water. Major contributions are shown along with the nature of the transitions.

| $\lambda$ [nm] | $f$ | Major contributions[a] | Nature of transition | Band |
|---|---|---|---|---|
| 515 | 0.0291 | β-HOMO−1→β-LUMO (0.68) | $\mathrm{Fe(d_\pi)–O(p_\pi)\rightarrow Fe(d_\pi)–O(p_\pi)}$ (Fe−O bond $\pi\rightarrow\pi^*$) | I |
| | | β-HOMO−2→β-LUMO+1 (−0.45) | | |
| | | β-HOMO−4→β-LUMO (−0.38) | $\mathrm{N_{amine}(p_\sigma^*)\rightarrow Fe(d_\pi)–O(p_\pi)}$ | |
| 462 | 0.0013 | α-HOMO−2→α-LUMO (0.59) | $\mathrm{Fe(d_\pi)–O(p_\pi^*)\rightarrow N_{amine}(p_\sigma^*)–Fe(d_{x^2-y^2})}$ | |
| | | α-HOMO→α-LUMO (0.42) | $\mathrm{N_{amine}(p_\sigma^*)\rightarrow N_{amine}(p_\sigma^*)–Fe(d_{x^2-y^2})}$ | |
| | | β-HOMO→β-LUMO+1 (-0.35) | $\mathrm{Fe(d_{xy})\rightarrow Fe(d_\pi)–O(p_\pi)}$ | |
| | | β-HOMO→β-LUMO+2 (-0.58) | $\mathrm{Fe(d_{xy})\rightarrow Fe(d_\pi)–O(p_\pi^*)}$ | |
| 447 | 0.0018 | α-HOMO−1→α-LUMO (0.61) | $\mathrm{Fe(d_\pi)–O(p_\pi^*)\rightarrow N_{amine}(p_\sigma^*)–Fe(d_{x^2-y^2})}$ | |
| | | β-HOMO→β-LUMO+3 (−0.57) | $\mathrm{Fe(d_{xy})\rightarrow Fe(d_\pi)–O(p_\pi^*)}$ | |
| 440 | 0.0028 | α-HOMO−2→α-LUMO (0.47) | $\mathrm{Fe(d_\pi)–O(p_\pi^*)\rightarrow N_{amine}(p_\sigma^*)–Fe(d_{x^2-y^2})}$ | II |
| | | α-HOMO→α-LUMO (0.30) | $\mathrm{N_{amine}(p_\sigma^*)\rightarrow N_{amine}(p_\sigma^*)–Fe(d_{x^2-y^2})}$ | |
| | | β-HOMO→β-LUMO+1 (0.35) | $\mathrm{Fe(d_{xy})\rightarrow Fe(d_\pi)–O(p_\pi)}$ | |
| | | β-HOMO→β-LUMO+2 (0.66) | $\mathrm{Fe(d_{xy})\rightarrow Fe(d_\pi)–O(p_\pi^*)}$ | |
| 429 | 0.0353 | β-HOMO−4→β-LUMO (0.83) | $\mathrm{N_{amine}(p_\sigma^*)\rightarrow Fe(d_\pi)–O(p_\pi)}$ | II |
| | | β-HOMO−2→β-LUMO+1 (-0.38) | $\mathrm{Fe(d_\pi)–O(p_\pi)\rightarrow Fe(d_\pi)–O(p_\pi)}$ (Fe−O bond $\pi\rightarrow\pi^*$) | |
| 380 | 0.0015 | α-HOMO−1→α-LUMO+1 (0.56) | $\mathrm{Fe(d_\pi)–O(p_\pi^*)\rightarrow O(p_\sigma^*)–Fe(d_{z^2})}$ | |
| | | β-HOMO−5→β-LUMO+1 (−0.48) | $\mathrm{N_{amine}(p_\sigma^*)\rightarrow Fe(d_\pi)–O(p_\pi)}$ | |
| 378 | 0.0129 | α-HOMO→α-LUMO+1 (−0.32) | $\mathrm{N_{amine}(p_\sigma^*)\rightarrow O(p_\sigma^*)–Fe(d_{z^2})}$ | |
| | | β-HOMO−5→β-LUMO (0.82) | $\mathrm{N_{amine}(p_\sigma^*)\rightarrow Fe(d_\pi)–O(p_\pi)}$ | |

[a] CI coefficients in parentheses.

optimized quintet-state geometry have mixed LMCT and MLCT character (mainly derived from $\mathrm{Fe(d_\pi)–O(p_\pi^*)\rightarrow N_{amine}(p_\sigma^*)–Fe(d_{x^2-y^2})}$ and $\mathrm{Fe(d_{xy})\rightarrow Fe(d_\pi)–O(p_\pi^*)}$ transitions), whereas the transitions at 447 and 441 nm in the PW91 optimized singlet-state geometry are solely of LMCT character (see above).

**Redox properties**: Because *trans*-dioxo ruthenium(VI) complexes are well-documented to be strong oxidants,[53] it is of interest to estimate the reduction potential of the $\mathrm{Fe^{VI/V}}$ couple for *trans*-$[\mathrm{Fe(O)_2(NH_3)_2(NMeH_2)_2}]^{2+}$. We thus optimized the geometries of *trans*-$[\mathrm{M(O)_2(NH_3)_2(NMeH_2)_2}]^{+}$ with both $S=\tfrac{1}{2}$ (doublet state) and $S=\tfrac{3}{2}$ (quartet state) using PW91. For calculations with the PW91 functional, the doublet state is lower in energy than the quartet state for all M (M = Fe, Ru, and Os; see Table 9). This is consistent with magnetic moments for *trans*-$[\mathrm{M(O)_2(14\text{-}TMC)}]^{+}$ of 1.93 and 1.89 $\mu_B$ for M = Ru,[27] and Os,[39] respectively, that is, a doublet ground-state electronic configuration. Structural parameters of the PW91 optimized doublet ground-state geometries of *trans*-$[\mathrm{M(O)_2(NH_3)_2(NMeH_2)_2}]^{+}$ are presented in Table 9.

Addition of an electron to *trans*-$[\mathrm{M^{VI}(O)_2(NH_3)_2(NMeH_2)_2}]^{2+}$ leads to elongation of the M−O bond, which is in accordance with the MO picture depicted in Figure 2 that the added electron goes to the antibonding $\pi$ orbitals of $\mathrm{M(d_\pi)–O(p_\pi^*)}$ character (LUMO or LUMO+1). Such a change in the M−O distance is the smallest for M = Fe (0.057–0.068 Å), but comparable for M = Ru and Os (0.073–0.076 and 0.075–0.078 Å for Ru and Os respectively). On one-electron reduction of *trans*-$[\mathrm{M(O)_2(NH_3)_2(NMeH_2)_2}]^{2+}$ to *trans*-$[\mathrm{M(O)_2(NH_3)_2(NMeH_2)_2}]^{+}$, the O-M-O angle remains essentially linear for M = Fe, but changes from a linear to a bent geometry when M = Ru and Os (see Tables 2 and 9). Bending of the O-M-O unit decreases the σ-bonding interactions between $\mathrm{M(d_{z^2})}$ and $\mathrm{O(p_\sigma)}$ orbitals and causes a greater elongation of the M−O bonds for M = Ru and Os.

Table 9. Optimized ground-state geometrical parameters of *trans*-$[\mathrm{M(O)_2(NH_3)_2(NMeH_2)_2}]^{+}$ from PW91 calculations and energy difference ($\Delta E_{\mathrm{Q-D}}$) between the optimized quartet and doublet ground states of *trans*-$[\mathrm{M(O)_2(NH_3)_2(NMeH_2)_2}]^{+}$ (M = Fe, Ru, Os).[a]

| M | $\Delta E_{\mathrm{Q-D}}$ [eV] | $r$(M=O) [Å][b] | $r(\mathrm{M{-}N_{amine}})$ [Å][b] | ∡(O-M-O) [°][b] |
|---|---|---|---|---|
| $\mathrm{Fe^V}$ | 0.63 (0.61) | 1.671 | 2.027 | 180 |
| | | | 2.063 | |
| | | 1.681 | 2.029 | |
| | | | 2.060 | |
| $\mathrm{Ru^V}$ | 1.33 (1.29) | 1.811 | 2.145 | 170 |
| | | | 2.184 | |
| | | 1.811 | 2.138 | |
| | | | 2.159 | |
| $\mathrm{Os^V}$ | 1.73 (1.66) | 1.837 | 2.160 | 171 |
| | | | 2.186 | |
| | | 1.837 | 2.149 | |
| | | | 2.167 | |

[a] $E_{\mathrm{Q-D}}=E(\text{quartet state})-E(\text{doublet state})$. The values in parentheses are thermal Gibbs free-energy differences. [b] Only the optimized doublet ground-state geometries are given. For the optimized quartet-state geometries, see Tables S55–S57 in the Supporting Information).

The reduction potentials of *trans*-$[\mathrm{M^{VI/V}(O)_2(NH_3)_2(NMeH_2)_2}]^{2+/+}$ couples were estimated by Equation (1) (see Computational Methods). If we relate the calculated Gibbs free-energy change to the reduction potential of +0.56 V versus NHE measured experimentally for the $\mathrm{Ru^{VI/V}}$ couple of *trans*-$[\mathrm{Ru(O)_2(14\text{-}TMC)}]^{2+}$[27] (Gibbs free-energy changes are listed in Table S58 in the Supporting Information), the reduction potential of the $\mathrm{Os^{VI/V}}$ couple of *trans*-$[\mathrm{Os(O)_2(NH_3)_2(NMeH_2)_2}]^{2+}$ would be estimated to be +0.01 V, which is consistent with the experimental data of +(0.048 ± 0.01) V (vs. NHE) found for *trans*-$[\mathrm{Os(O)_2(14\text{-}TMC)}]^{2+/+}$.[37] The corresponding $\mathrm{Fe^{VI/V}}$ couple of *trans*-$[\mathrm{Fe(O)_2(NH_3)_2(NMeH_2)_2}]^{2+}$ is estimated to be +1.30 V versus NHE, that is, it is a strong oxidant capable even of oxidizing solvent water, based on energetics. On this basis, it is conceivable that cationic dioxo iron(VI) complexes supported by saturated amine ligands could only be prepared in redox-inactive reaction media.

Because a quintet state is predicted to be the ground state for *trans*-$[Fe(O)_2(NH_3)_2(NMeH_2)_2]^{2+}$ with hybrid DFs B3LYP and PBE1PBE, we have also optimized the geometry of *trans*-$[M(O)_2(NH_3)_2(NMeH_2)_2]^+$ (M = Fe and Ru) by employing B3LYP. As in the case of *trans*-$[Fe(O)_2(NH_3)_2(NMeH_2)_2]^{2+}$, the high-spin quartet state of *trans*-$[Fe(O)_2(NH_3)_2(NMeH_2)_2]^+$ is more stable than the low-spin doublet state by about 0.28 eV, whereas in the case of *trans*-$[Ru(O)_2(NH_3)_2(NMeH_2)_2]^+$ the low-spin doublet state is, as predicted from PW91 calculations, the more stable state (by 0.74 eV; see Table 10).

Table 10. Optimized ground-state geometrical parameters of *trans*-$[M(O)_2(NH_3)_2(NMeH_2)_2]^+$ from B3LYP calculations and energy difference ($\Delta E_{Q-D}$) between the optimized quartet and doublet ground states of *trans*-$[M(O)_2(NH_3)_2(NMeH_2)_2]^+$ (M = Fe, Ru).[a]

| M | $\Delta E_{Q-D}$ [eV] | $r$(M=O) [Å][b] | $r$(M−N$_{amine}$) [Å][b] | ∢(O-M-O) [°][b] |
|---|---|---|---|---|
| Fe | −0.28 (−0.35) | 1.756 | 2.075 | 173 |
| | | | 2.072 | |
| | | 1.746 | 2.051 | |
| | | | 2.080 | |
| Ru | 0.74 (0.67) | 1.796 | 2.158 | 169 |
| | | | 2.196 | |
| | | 1.795 | 2.152 | |
| | | | 2.169 | |

[a] $E_{Q-D} = E$(quartet state)−$E$(doublet state). The values in parentheses are thermal Gibbs free-energy differences. [b] Only the optimized ground-state geometries are given (doublet for M = Ru and quartet for M = Fe).

As the β-LUMO of *trans*-$[Fe(O)_2(NH_3)_2(NMeH_2)_2]^{2+}$ in the B3LYP optimized quintet state has both Fe−O π bonding and antibonding character (see Figure 1 for the MO surfaces), addition of an electron to this LUMO would result in elongation of one Fe−O bond and shortening of the other (1.748 and 1.761 Å in the quintet state, and 1.756 and 1.746 Å in the quartet state). Because the LUMO does not have significant amine character, the Fe−N$_{amine}$ distances only increase slightly (by ca. 0.01 Å). For *trans*-$[Ru(O)_2(NH_3)_2(NMeH_2)_2]^{2+}$, the geometrical parameters are all in agreement with the PW91 results: the electron is added to the antibonding Ru−O orbital and leads to elongation of both Ru−O bonds. Since the change in charge distribution for the two systems *trans*-$[Fe(O)_2(NH_3)_2(NMeH_2)_2]^{2+}$ and *trans*-$[Ru(O)_2(NH_3)_2(NMeH_2)_2]^{2+}$ on one-electron reduction are not the same from the B3LYP calculations, we did not estimate the reduction potential of *trans*-$[Fe(O)_2(NH_3)_2(NMeH_2)_2]^{2+}$ from the Gibbs free energies obtained from B3LYP calculations by using Equation (1).

**Detection of $[Fe(qpy)(O)_2]^{n+}$ ions in the gas phase by high-resolution ESI-MS/MS**: The reaction of $[Fe^{II}(qpy)(CH_3CN)_2](ClO_4)_2$ with $PhI(OAc)_2$ in acetonitrile was followed by ESI-MS for 15 min. New peaks at *m/z* 475.0758 (peak separation of 1 mass unit), 459.0416 (peak separation of 1 mass unit), 237.5347 (peak separation of 0.5 mass units), and 229.54 (peak separation of 0.5 mass units) were detected in positive-ion mode. Based on accurate mass measurement and isotopic-pattern matching, the elemental composition of the most abundant isotopic ion peaks at *m/z* 475.0758 (Figure 4a) and 237.5347 (Figure 4b) were determined to be $[C_{25}H_{17}N_5O_2{}^{56}Fe]^+$ (theoretical mass = 475.0732) and $[C_{25}H_{17}N_5O_2{}^{56}Fe]^{2+}$ (theoretical mass = 237.5366), which are consistent with the formulations $[Fe(qpy)(O)_2]^+$ and $[Fe(qpy)(O)_2]^{2+}$, respectively. Experiments involving collision-induced dissociation of these $[Fe(qpy)(O)_2]^{n+}$ ions further confirmed these formulations (Figure 5). The isotopic ion peaks at *m/z* 459.0509 and 229.5355 were determined to be $[C_{25}H_{17}N_5O^{56}Fe]^+$ (theoretical mass = 459.0783) and $[C_{25}H_{17}N_5O^{56}Fe]^{2+}$ (theoretical mass = 229.5391), which are consistent with the formulations $[Fe(qpy)O]^+$ and [Fe-

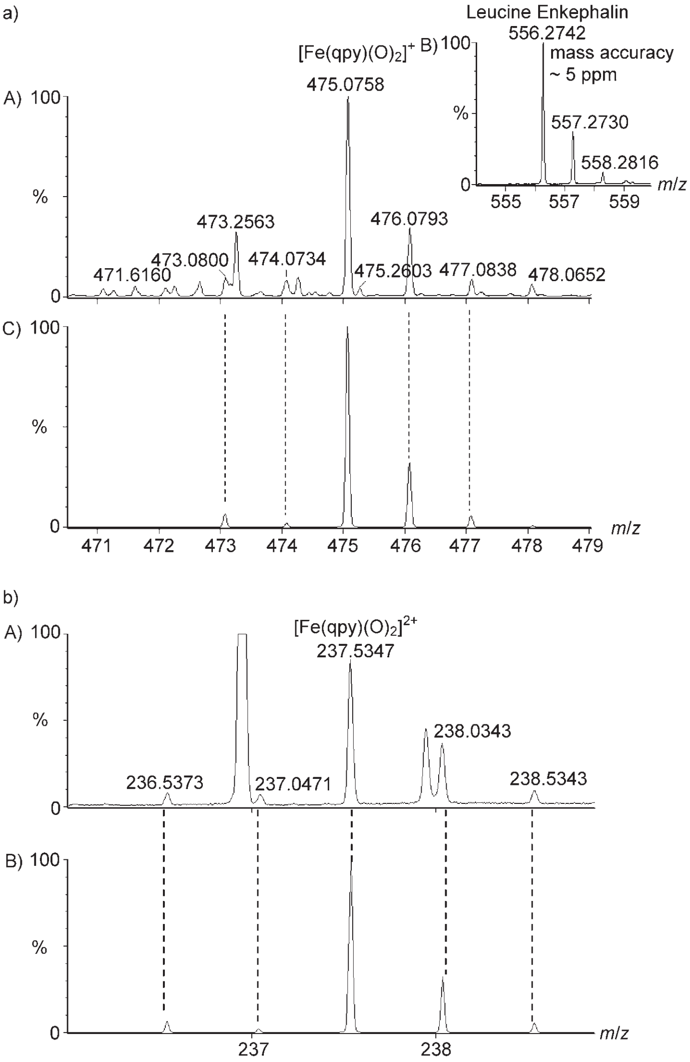

Figure 4. a) ESI-MS measurements on $[Fe(qpy)(O)_2]^+$. A) Accurate mass measurement. B) Reference mass of Leucine Enkephalin. C) Isotopic pattern of $[C_{25}H_{17}N_5O_2Fe]^+$. b) ESI-MS measurements on $[Fe(qpy)(O)_2]^{2+}$. A) Accurate mass measurement. B) Isotopic pattern of $[C_{25}H_{17}N_5O_2Fe]^{2+}$.

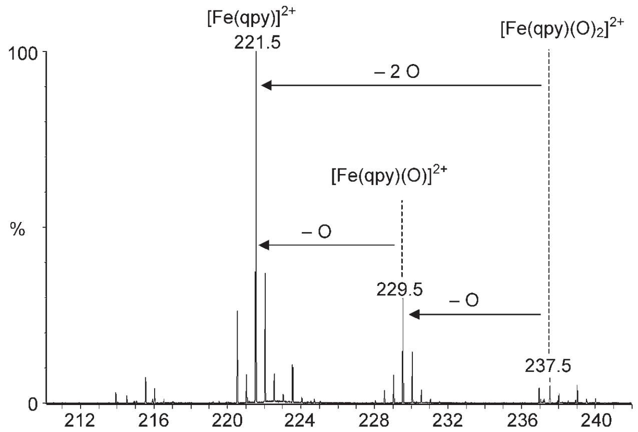

Figure 5. Collision-induced dissociation of [Fe(qpy)(O)$_2$]$^{2+}$ recorded at a collision energy of 25 eV (laboratory frame).

(qpy)O]$^{2+}$, respectively (see Figures S1 and S2 in the Supporting Information). The differences between the experimental and theoretical masses for these [Fe(qpy)(O)$_m$]$^{n+}$ ($m=1, 2$; $n=1, 2$) ion peaks are less than 6 ppm.

We examined the formation of [Fe(qpy)(O)$_m$]$^{n+}$ ($m=1, 2$; $n=1, 2$) ions in the gas phase (see Figure S3 in the Supporting Information). The abundance of these ions during the first 10 min was in the order [Fe(qpy)O]$^{+}$ > [Fe(qpy)O]$^{2+}$ ≈ [Fe(qpy)(O)$_2$]$^{+}$ ≫ [Fe(qpy)(O)$_2$]$^{2+}$. The signal intensity of [Fe(qpy)(O)$_2$]$^{2+}$ was at least eight times less than that of [Fe(qpy)(O)$_2$]$^{+}$ and thirty times less than that of [Fe(qpy)O]$^{+}$. We attribute this finding to the reactive nature of [Fe(qpy)(O)$_2$]$^{2+}$, which could be decomposed to [Fe(qpy)(O)$_2$]$^{+}$, [Fe(qpy)O]$^{2+}$, and [Fe(qpy)O]$^{+}$.

## Conclusion

We have examined the properties of *trans*-dioxo metal complexes supported by saturated amine ligands, *trans*-[M(O)$_2$(NH$_3$)$_2$(NMeH$_2$)$_2$]$^{2+}$ (M = Fe, Ru, and Os), using a DFT/TDDFT approach. Electronic structures, spectroscopic data, and reduction potentials were computed, analyzed, and compared. Different ground-state structures were obtained when different types of DFs were used in the calculations on *trans*-[Fe(O)$_2$(NH$_3$)$_2$(NMeH$_2$)$_2$]$^{2+}$: pure GGAs and meta-GGAs predicted a singlet d$^2$ ground state, and hence, the existence of *trans*-dioxo iron(VI), whereas with hybrid DFs, a quintet state is predicted to be the most stable. We favor the PW91 results on *trans*-[Fe(O)$_2$(NH$_3$)$_2$(NMeH$_2$)$_2$]$^{2+}$ for the following reasons:

1) Hybrid DFs tend to favor high-spin states.
2) Another DF, namely, OLYP, also known to favor more spin polarized descriptions and has been successful in predicting the spin-state energetics of a number of Fe$^{II}$ systems that contain ligands with different ligand-field strengths,[54] also gave a singlet d$^2$ ground state for *trans*-[Fe(O)$_2$(NH$_3$)$_2$(NMeH$_2$)$_2$]$^{2+}$.
3) The well-separated Fe−O bonding and antibonding MOs are singly occupied in the ground quintet state, whereas the former is fully filled and the latter is empty in the singlet state obtained from the hybrid DF optimization.

These reasons lend credence to the PW91 results that *trans*-[M(O)$_2$(NH$_3$)$_2$(NMeH$_2$)$_2$]$^{2+}$ has a d$^2$ singlet ground state for M = Fe, Ru, and Os. Hence, we conclude that *trans*-dioxo iron(VI) could be stabilized in an octahedral environment with saturated amine equatorial ligands, at least theoretically. Interestingly, although different DFs predicted different spin ground states of *trans*-[Fe(O)$_2$(NH$_3$)$_2$(NMeH$_2$)$_2$]$^{2+}$, the transition energies found with pure GGA PW91 and hybrid DF B3LYP are similar, though the nature of the lowest transition is not the same: PW91 predicted it to be of LMCT character, whereas B3LYP predicted a π(Fe−O)→π*(Fe−O) transition. As the Fe−O bond is predicted to be the weakest and the redox potential of *trans*-[Fe(O)$_2$(NH$_3$)$_2$(NMeH$_2$)$_2$]$^{2+}$ is estimated to be about +1.30 V versus NHE, if dioxo iron(VI) species could be generated in solution, they may function as a class of versatile oxygen-transfer agents. Indeed, after the completion of this work, we were able to detect [Fe(qpy)(O)$_2$]$^{n+}$ ($n=1, 2$) ions in the gas phase by high-resolution ESI-MS/MS.

## Computational and Experimental Section

**Computational details**: Despite many successful cases of using DFT to probe the electronic structures of high-valent Fe complexes, DFT is far from infallible, in particular when the ancillary ligands are noninnocent. For instance, Por and Cor are more appropriately formulated as π-cation radicals in Fe(Por)F$_2$[55] and Fe(Cor)Cl,[56] respectively. In the present work, we chose simple amines, NH$_3$ and NMeH$_2$, as ancillary ligands. As modeling of the relative spin-state energetics by DFT methods remains elusive,[32,54,57] the calculations on *trans*-[M(O)$_2$(NH$_3$)$_2$(NMeH$_2$)$_2$]$^{n+}$ (M = Fe, Ru, and Os) were performed in different spin states ($S=0, 1, 2$ for $n=2$; $S=\frac{1}{2}$ and $\frac{3}{2}$ for $n=1$) with the Gaussian 03 program package.[58] The $z$ axis is defined along the O=M=O unit, and the $x$ and $y$ axes are set along the two N$_{\text{amine}}$-M-N$_{\text{amine}}$ axes. Two different amine ligands, NH$_3$ and NMeH$_2$, along the $x$ and $y$ axes, respectively, were chosen to lift the degeneracy of the metal d$_{xz}$ and d$_{yz}$ orbitals because a spin state with only one of these two degenerate orbitals occupied would be multiconfigurational in nature. As the DFT method is a single-reference based method, these two d$_\pi$ (d$_{xz}$ and d$_{yz}$) orbitals are required to be nondegenerate in the calculations.

The accuracy of DFT calculations depends on the functional and basis set used. Therefore, we employed different exchange-correlation DFs, which included 1) GGAs PW91,[59–61] BP86,[62,63] and OLYP;[64,65] 2) meta-GGAs VSXC[66] and HCTH407;[67] and 3) hybrid DFs B3LYP[68,69] and PBE1PBE.[70–72] Two different basis sets were used for each DF: the

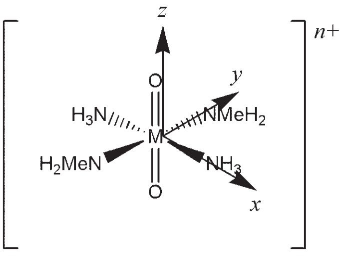

smaller 6-31G* basis set (double-zeta quality with polarization functions on non-H atoms)[73,74] and the larger 6-311+G*[75,76] (triple-zeta quality with both polarization and diffuse functions added to the non-hydrogen atoms) for all atoms except transition metal atoms, which were described by the Stuttgart relativistic small-core effective-core potentials with their accompanying basis sets in all calculations.[77,78]

Full geometry optimizations were performed without symmetry constraints followed by frequency calculations to ensure that the optimized structures were true energy minima. Restricted formalism was used for the closed-shell spin state, whereas an unrestricted formalism was used for the open-shell spin states. Electronic structures of the complexes studied in the present work were also investigated by using the natural bond orbital (NBO) approach.[79] Spin-allowed excitation energies of the model complexes were computed at the optimized ground-state structures in solvent water by using the TDDFT method implemented in Gaussian 03.[80,81] Solvation effects were taken into account by the CPCM.[82,83] The absorption spectra were simulated with Gaussian functions with a fwhm of 3000 $\mathrm{cm}^{-1}$ for all electronic transitions with $\lambda >$ 200 nm by using GaussSum[84] to allow direct comparison with the experimental data.

The reduction potential ($E^0$) for the *trans*-$[\mathrm{M(O)_2(NH_3)_2(NMeH_2)_2}]^{2+/+}$ ($\mathrm{m}^{2+/+}$) couples (M=Fe, Ru, and Os) are related to the Gibbs free-energy $G$ change of the monocationic ($\mathrm{m}^+$) and dicationic ($\mathrm{m}^{2+}$) complexes by Equation (1):

$$E^0 = G(\mathrm{m}^+) - G(\mathrm{m}^{2+}) + C \qquad (1)$$

$G(\mathrm{m}^+)$ and $G(\mathrm{m}^{2+})$ were calculated at the respective optimized ground-state structures of $\mathrm{m}^+$ and $\mathrm{m}^{2+}$, respectively, in solvent water with a default temperature and pressure of 298 K and 1 atm. $C$ is a constant that is related to the reference electrode used.

**Experimental section**: $[\mathrm{Fe^{II}(qpy)(CH_3CN)_2}](\mathrm{ClO_4})_2$ was prepared according to a literature method.[85] Positive ESI mass spectra were obtained from a Waters Micromass Q-Tof Premier quadrupole time-of-flight tandem mass spectrometer (Waters Corporation, Milford, USA). A solution of $[\mathrm{Fe^{II}(qpy)(CH_3CN)_2}](\mathrm{ClO_4})_2$ (1.5 mg, 2.1 μmol) in acetonitrile was treated with $\mathrm{PhI(OAc)_2}$ (2.67 mg, 8.3 μmol) in a ratio of 1:4. The reaction mixture was introduced into the ESI source by a syringe pump operating at a flow rate of 10 $\mu\mathrm{L\,min}^{-1}$ after 30 s of mixing. For accurate mass measurements, an internal reference compound, namely, Leucine Enkephalin, was diluted 200 times and then introduced into the ESI source through an independent electrospray probe to avoid any chemical interference with the reaction mixture. The mass resolution was set at about 8000 (full width at half-height), and mass accuracy was within 10 ppm. The TOF-MS mass spectra were acquired in the mass range of 100–1200 Th with an accumulation time of 1 s and interscan time of 0.1 s.

In the MS/MS experiment, the parent ion at $m/z$ 475.0 corresponding to $[\mathrm{Fe(qpy)(O)_2}]^+$ and 237.5 corresponding to $[\mathrm{Fe(qpy)(O)_2}]^{2+}$ were separately mass-selected by the first quadrupole mass analyzer (operating at about unit mass resolution). The selected ion was transmitted into a T-wave collision cell (filled with argon gas at $7.01\times10^{-3}$ Torr, measured in the quadrupole mass-analyzer housing) where it underwent collision-induced dissociation at a collision energy of 25 eV (laboratory frame). The parent ion and fragment ions were mass-analyzed by the TOF mass analyzer and detected by a multichannel plate (MCP) detector at 1.8 kV. The MS/MS spectrum was obtained by averaging about 200 scans.

## Acknowledgements

This work was supported by the Small Project Funding Program of the University of Hong Kong and the University Grants Committee of the Hong Kong SAR of China (Area of Excellence Scheme, AoE/P-10/01). We are thankful to Dr. Kwan-Ming Ng for his assistance and discussions on ESI-MS in this work.

[1] M. Costas, M. P. Mehn, M. P. Jensen, L. Que, Jr., *Chem. Rev.* **2004**, *104*, 939.
[2] S. V. Kryatov, E. V. Rybak-Akimova, S. Schindler, *Chem. Rev.* **2005**, *105*, 2175.
[3] P. Nordlund in *Handbook on Metalloproteins* (Eds.: I. Bertini, A. Sigel, H. Sigel), Marcel Dekker, New York, **2001**, p. 461.
[4] B. Meunier, S. P. de Visser, S. Shaik, *Chem. Rev.* **2004**, *104*, 3947.
[5] E. I. Solomon, T. C. Brunold, M. I. Davis, J. N. Kemsley, S.-K. Lee, N. Lehnert, F. Neese, A. J. Skulan, Y.-S. Yang, J. Zhou, *Chem. Rev.* **2000**, *100*, 235.
[6] M. Sono, M. P. Roach, E. D. Coulter, J. H. Dawson, *Chem. Rev.* **1996**, *96*, 2841.
[7] M. Newcomb, R. E. P. Chandrasena, *Biochem. Biophys. Res. Commun.* **2005**, *338*, 394.
[8] J. C. Price, E. W. Barr, B. Tirupati, J. M. Bollinger, Jr., C. Krebs, *Biochemistry* **2003**, *42*, 7497.
[9] J.-U. Rohde, J.-H. In, M. H. Lim, W. W. Brennessel, M. R. Bukowski, A. Stubna, E. Munck, W. Nam, L. Que, Jr., *Science* **2003**, *299*, 1037.
[10] M. H. Lim, J.-U. Rohde, A. Stubna, M. R. Bukowski, M. Costas, R. Y. N. Ho, E. Munck, W. Nam, L. Que, Jr., *Proc. Natl. Acad. Sci. USA* **2003**, *100*, 3665.
[11] A. Decker, J.-U. Rohde, L. Que, Jr., E. I. Solomon, *J. Am. Chem. Soc.* **2004**, *126*, 5378.
[12] E. J. Klinker, J. Kaizer, W. W. Brennessel, N. L. Woodrum, C. J. Cramer, L. Que, Jr., *Angew. Chem.* **2005**, *117*, 3756; *Angew. Chem. Int. Ed.* **2005**, *44*, 3690.
[13] K. Chen, L. Que, Jr., *J. Am. Chem. Soc.* **2001**, *123*, 6327.
[14] A. Bassan, M. R. A. Blomberg, P. E. M. Siegbahn, L. Que, Jr., *J. Am. Chem. Soc.* **2002**, *124*, 11056.
[15] R. Zhang, R. E. P. Chandrasena, E. Martinez II, J. H. Horner, M. Newcomb, *Org. Lett.* **2005**, *7*, 1193.
[16] D. Harischandra, R. Zhang, M. Newcomb, *J. Am. Chem. Soc.* **2005**, *127*, 13776.
[17] F. Tiago de Oliveira, A. Chanda, D. Banerjee, X. Shan, S. Mondal, L. Que, Jr., E. L. Bominaar, E. Muenck, T. J. Collins, *Science* **2006**, *315*, 835.
[18] M. L. Hoppe, E. O. Schlemper, R. K. Murmann, *Acta Crystallogr. Sect. B* **1982**, *38*, 2237.
[19] M. Herren, H. U. Gudel, *Inorg. Chem.* **1992**, *31*, 3683.
[20] M. Atanasov, H. Adamsky, K. Eifert, *J. Solid State Chem.* **1997**, *128*, 1.
[21] K. Wissing, M. T. Barriuso, J. A. Aramburu, M. Moreno, *J. Chem. Phys.* **1999**, *111*, 10217.
[22] A. Dey, A. Ghosh, *J. Am. Chem. Soc.* **2002**, *124*, 3206.
[23] W. P. Griffith, *Chem. Soc. Rev.* **1992**, *21*, 179.
[24] E. J. Lebeau, T. J. Meyer, *Inorg. Chem.* **1999**, *38*, 2174.
[25] A. Dovletoglou, T. J. Meyer, *J. Am. Chem. Soc.* **1994**, *116*, 215.
[26] C.-M. Che, W.-T. Tang, C.-K. Li, *J. Chem. Soc. Dalton Trans.* **1990**, 3735.
[27] C.-M. Che, T. F. Lai, K.-Y. Wong, *Inorg. Chem.* **1987**, *26*, 2289.
[28] V. W. W. Yam, C.-M. Che, *Coord. Chem. Rev.* **1990**, *97*, 93.
[29] J. F. Berry, E. Bill, E. Bothe, S. D. George, B. Mienert, F. Neese, K. Wieghardt, *Science* **2006**, *312*, 1937.
[30] I. Wasbotten, A. Ghosh, *Inorg. Chem.* **2006**, *45*, 4910.
[31] A. Ghosh, *J. Inorg. Biochem.* **2006**, *100*, 419.
[32] A. Ghosh, *J. Biol. Inorg. Chem.* **2006**, *11*, 712.
[33] P. Hummel, J. R. Winkler, H. B. Gray, *Dalton Trans.* **2006**, 168.
[34] I. Demachy, Y. Jean, *Inorg. Chem.* **1996**, *35*, 5027.
[35] I. Demachy, Y. Jean, *Inorg. Chem.* **1997**, *36*, 5956.
[36] C.-M. Che, K.-Y. Wong, C.-K. Poon, *Inorg. Chem.* **1985**, *24*, 1797.
[37] C. Kelly, D. J. Szalda, C. Creutz, H. A. Schwarz, N. Sutin, *Inorg. Chim. Acta* **1996**, *243*, 39.
[38] S. Schindler, E. W. Castner, Jr., C. Creutz, N. Sutin, *Inorg. Chem.* **1993**, *32*, 4200.
[39] C.-M. Che, W.-K. Cheng, V. W. W. Yam, *J. Chem. Soc. Dalton Trans.* **1990**, 3095.

[40] As the electronic structures are all similar within the pure GGAs and meta-GGAs considered in the present work and among the hybrid DFs, B3LYP, and PBE1PBE, we present only the PW91 results.

[41] J. M. Poblet, X. Lopez, C. Bo, *Chem. Soc. Rev.* **2003**, *32*, 297.

[42] A. Decker, E. I. Solomon, *Angew. Chem.* **2005**, *117*, 2292; *Angew. Chem. Int. Ed.* **2005**, *44*, 2252.

[43] P. Pyykko, *Chem. Rev.* **1988**, *88*, 563.

[44] W. P. Griffith, *J. Chem. Soc. A* **1969**, 211.

[45] T. C. W. Mak, C.-M. Che, K.-Y. Wong, *J. Chem. Soc. Dalton Trans.* **1985**, 966.

[46] A. M. El-Hendawy, W. P. Griffith, *J. Chem. Soc. Dalton Trans.* **1989**, 901.

[47] B. A. Moyer, T. J. Meyer, *Inorg. Chem.* **1981**, *20*, 436.

[48] G. L. Gustev, B. K. Rao, P. Jena, *J. Phys. Chem. A* **2000**, *104*, 11961.

[49] V. M. Miskowski, H. B. Gray, M. D. Hopkins, *Adv. Transition Met. Chem.* **1996**, *1*, 159.

[50] C. Sartori, W. Preetz, *Z. Anorg. Allg. Chem.* **1989**, *572*, 151.

[51] An intense band is calculated at 236 nm ($f=0.2359$) for $[Ru(O)_2(NH_3)_2(NMeH_2)_2]^{2+}$ (see Table S51 in the Supporting Information). This is derived from the HOMO$-4\rightarrow$LUMO$+2$ transition and compares well with the band at about 220–260 nm in *trans*-$[Ru(O)_2L]^{2+}$ (L = 14-TMC, 15-TMC, and 16-TMC).[27] Since this transition also involves the LUMO$+2$ orbital, it is expected that the effect of macrocycle ring size also applies to this transition.

[52] Because GaussSum 1.0 does not create UV/Vis spectra from unrestricted calculations, we did not simulate the UV/Vis spectrum of *trans*-$[Fe(O)_2(NH_3)_2(NMeH_2)_2]^{2+}$ in the B3LYP optimized quintet-state geometry.

[53] C.-M. Che, V. W. W. Yam, *Adv. Mater. Sci. Technol. Adv. Transition Met. Chem.* **1996**, *1*, 209.

[54] G. Ganzenmuller, N. Berkaine, A. Fouqueau, M. E. Casida, M. Reiher, *J. Chem. Phys.* **2005**, *122*, 234321/1.

[55] A. Ghosh, P. R. Taylor, *J. Chem. Theory Comput.* **2005**, *1*, 597.

[56] I. Wasbotten, A. Ghosh, *Inorg. Chem.* **2006**, *45*, 4914.

[57] O. Salomon, M. Reiher, B. A. Hess, *J. Chem. Phys.* **2002**, *117*, 4729.

[58] Gaussian 03, Revision B.05, M. J. Frisch, G. W. Trucks, H. B. Schlegel, G. E. Scuseria, M. A. Robb, J. R. Cheeseman, J. A. Montgomery, Jr., T. Vreven, K. N. Kudin, J. C. Burant, J. M. Millam, S. S. Iyengar, J. Tomasi, V. Barone, B. Mennucci, M. Cossi, G. Scalmani, N. Rega, G. A. Petersson, H. Nakatsuji, M. Hada, M. Ehara, K. Toyota, R. Fukuda, J. Hasegawa, M. Ishida, T. Nakajima, Y. Honda, O. Kitao, H. Nakai, M. Klene, X. Li, J. E. Knox, H. P. Hratchian, J. B. Cross, V. Bakken, C. Adamo, J. Jaramillo, R. Gomperts, R. E. Stratmann, O. Yazyev, A. J. Austin, R. Cammi, C. Pomelli, J. W. Ochterski, P. Y. Ayala, K. Morokuma, G. A. Voth, P. Salvador, J. J. Dannenberg, V. G. Zakrzewski, S. Dapprich, A. D. Daniels, M. C. Strain, O. Farkas, D. K. Malick, A. D. Rabuck, K. Raghavachari, J. B. Foresman, J. V. Ortiz, Q. Cui, A. G. Baboul, S. Clifford, J. Cioslowski, B. B. Stefanov, G. Liu, A. Liashenko, P. Piskorz, I. Komaromi, R. L. Martin, D. J. Fox, T. Keith, M. A. Al-Laham, C. Y. Peng, A. Nanayakkara, M. Challacombe, P. M. W. Gill, B. Johnson, W. Chen, M. W. Wong, C. Gonzalez, J. A. Pople, Gaussian, Inc., Wallingford CT, **2004**.

[59] J. P. Perdew in *Electronic Structure of Solids '91* (Eds.: P. Ziesche, H. Eschrig), Akademie Verlag, Berlin, **1991**.

[60] J. P. Perdew, J. A. Chevary, S. H. Vosko, K. A. Jackson, M. R. Pederson, D. J. Singh, C. Fiolhais, *Phys. Rev. B* **1992**, *46*, 6671.

[61] J. P. Perdew, J. A. Chevary, S. H. Vosko, K. A. Jackson, M. R. Pederson, D. J. Singh, C. Fiolhais, *Phys. Rev. B* **1993**, *48*, 4978.

[62] J. P. Perdew, *Phys. Rev. B* **1986**, *33*, 8822.

[63] A. D. Becke, *Phys. Rev. A* **1988**, *38*, 3098.

[64] N. C. Handy, A. J. Cohen, *Mol. Phys.* **2001**, *99*, 403.

[65] C. Lee, W. Yang, R. G. Parr, *Phys. Rev. B* **1988**, *37*, 785.

[66] T. van Voorhis, G. E. Scuseria, *J. Chem. Phys.* **1998**, *109*, 400.

[67] F. A. Hamprecht, A. J. Cohen, D. J. Tozer, N. C. Handy, *J. Chem. Phys.* **1998**, *109*, 6264.

[68] A. D. Becke, *J. Chem. Phys.* **1993**, *98*, 1372.

[69] P. J. Stephens, F. J. Devlin, C. F. Chabalowski, M. J. Frisch, *J. Phys. Chem.* **1994**, *98*, 11623.

[70] J. P. Perdew, Y. Wang, *Phys. Rev. B* **1992**, *45*, 13244.

[71] J. P. Perdew, K. Burke, M. Ernzerhof, *Phys. Rev. Lett.* **1996**, *77*, 3865.

[72] M. Ernzerhof, G. E. Scuseria, *J. Chem. Phys.* **1999**, *110*, 5029.

[73] M. M. Francl, W. J. Petro, W. J. Hehre, J. S. Binkley, M. S. Gordon, D. J. DeFree, J. A. Pople, *J. Chem. Phys.* **1982**, *77*, 3654.

[74] P. C. Hariharan, J. A. Pople, *Theor. Chim. Acta* **1973**, *28*, 213.

[75] R. Krishnan, J. S. Binkley, R. Seeger, J. A. Pople, *J. Chem. Phys.* **1980**, *72*, 650.

[76] T. Clark, J. Chandrasekhar, G. W. Spitznagel, P. v. R. Schleyer, *J. Comput. Chem.* **1983**, *4*, 294.

[77] D. Andrae, U. Haeussermann, M. Dolg, H. Stoll, H. Preuss, *Theor. Chim. Acta* **1990**, *77*, 123.

[78] M. Dolg, U. Wedig, H. Stoll, H. Preuss, *J. Chem. Phys.* **1987**, *86*, 866.

[79] A. E. Reed, L. A. Curtiss, F. Weinhold, *Chem. Rev.* **1988**, *88*, 899.

[80] R. E. Stratmann, G. E. Scuseria, M. J. Frisch, *J. Chem. Phys.* **1998**, *109*, 8128.

[81] M. E. Casida, *Recent Advances in Density Functional Methods*, Part 1, World Scientific, Singapore, **1995**.

[82] V. Barone, M. Cossi, J. Tomasi, *J. Chem. Phys.* **1997**, *107*, 3210.

[83] J. Tomasi, M. Persico, *Chem. Rev.* **1994**, *94*, 2027.

[84] GaussSum 1.0, N. M. O'Boyle, J. G. Vos, Dublin City University, **2005**; available at http://gausssum.sourceforge.net.

[85] E. L.-M. Wong, G.-S. Fong, C.-M. Che, N. Zhu, *Chem. Commun.* **2005**, 4578.

Received: October 5, 2007